

Upper Atmosphere Responses to the 2022 Hunga Tonga-Hunga Ha’apai Volcanic Eruption via Acoustic-Gravity Waves and Air-Sea Interaction

Qinzeng Li^{1,5}, Jiyao Xu^{1,2*}, Aditya Riadi Gusman³, Hanli Liu⁴, Wei Yuan^{1,5}, Weijun Liu^{1,5},
Yajun Zhu^{1,5}, and Xiao Liu⁶

1. State Key Laboratory of Space Weather, National Space Science Center, Chinese Academy of
Sciences, Beijing, 100190, China

2. School of Astronomy and Space Science, University of Chinese Academy of Science, Beijing,
100049, China

3. GNS Science, Lower Hutt, New Zealand

4. High Altitude Observatory, National Center for Atmospheric Research, Boulder, Colorado,
USA

5. Hainan National Field Science Observation and Research Observatory for Space Weather, National
Space Science Center, Chinese Academy of Sciences, Beijing, 100190, China

6. School of Mathematics and Information Science, Henan Normal University, Xinxiang, China

Corresponding author: Jiyao Xu (jyxu@swl.ac.cn)

18 Abstract

19 Multi-group of strong atmospheric waves (wave packets #1-#5) over China associated
20 with the 2022 Hunga Tonga–Hunga Ha’apai (HTHH) volcano eruptions were observed in the
21 mesopause region using a ground-based airglow imager network. The horizontal phase speed
22 of wave packet #1 and ~~wave packet~~ #2 is approximately 312–309 m/s and 238–236 m/s
23 respectively, which is consistent with Lamb wave L0 mode and L1 mode from theoretical
24 prediction. The amplitude of the lamb wave L1 mode is larger than that of L0 mode. The wave
25 fronts of Lamb wave L0 and L1 below the lower thermosphere are vertical, while the wave
26 fronts of L0 mode tilt forward above exhibiting internal wave characteristics, which show
27 good agreement with the theoretical results. Two types of tsunamis were simulated, one type
28 of tsunami is induced by the atmospheric pressure wave (TIAPW) and the other type tsunami
29 is directly induced by the Tonga volcano eruption (TITVE). From backward ray tracing
30 analysis, the TIAPW and TITVE were likely the sources of the ~~acoustic-gravity waves (AGWs)~~
31 ~~accompanying~~ wave packet ~~#2–3~~ and wave packets #4-5, respectively. The scale of tsunamis
32 near the coast is very consistent with the atmospheric AGWs observed by the airglow network.
33 The AGWs triggered by TITVE propagate nearly 3000 km inland with the support of duct ~~and~~
34 ~~persist for about 4.5 hr and almost covers the Chinese Mainland.~~ The atmospheric pressure
35 wave can directly affect the upper atmosphere, and can also be coupled with the upper
36 atmosphere through the indirect way of generating tsunami and subsequently tsunami
37 generating AGWs, which will provide a new understanding of the coupling between ocean and
38 atmosphere.

1. Introduction

Hunga Tonga–Hunga Ha’apai (HTHH) volcano, which erupted at 04:14:45 UT on January 15, 2022, produced the largest volcanic eruption in terms of energy release of a single event since the Krakatoa volcanic eruption (Symons, 1888) in 1883. This volcanic eruption triggered broad spectrum atmospheric disturbances (Adam, 2022; Duncombe, 2022; Wright et al., 2022), including Lamb waves (~~Kanamori and Given, 1983~~, Zhang et al., 2022), acoustic waves, gravity waves (GWs) (~~Fritts and Alexander, 2003~~; Liu et al., 2022), and shock waves (Astafyeva et al., 2022). In addition, the travelling ionospheric disturbances (TIDs) caused by this volcanic eruption have also been reported (Themens et al., 2022; Lin et al., 2022).

Lamb waves are external wave propagating along Earth’s surface at the speed of sound (Beer, 1974). They are non-dispersive or nearly non-dispersive (Francis, 1973) and can propagate horizontally over long distances. Lamb wave mainly occupies the troposphere, and its perturbation pressure decays exponentially with height (Yeh and Liu, 1974). The Lamb waves excited by the Tonga volcano eruptions went around the Earth several times (Amores et al., 2022; Duncombe, 2022; ~~Amores et al., 2022~~). Sepúlveda found that the wind field strongly affects the morphology and propagation of Lamb wave. Liu et al. (2023) reproduced the Lamb wave L0 and L1 modes consistently with theoretical predictions (Francis, 1973) using high-resolution Whole Atmosphere Community Climate Model with thermosphere/ionosphere extension (WACCM-X). Li et al. (2023) identified Lamb wave L1 mode ~~from GNSS-TEC analysis using phase-leveling amplitude technology~~ based on global navigation satellite system (GNSS)- total electron content (TEC). Poblet et

al. (2023) reported that the strong perturbations in the horizontal wind field is caused by lamb wave L1 mode associated with the 2022 HTHH volcano eruption.

Acoustic-gravity waves (AGWs) are mechanical waves in compressible fluids in a gravity field (Gossard and Hooke, 1975). If the frequencies are much larger than the buoyancy frequency, AGWs tend towards acoustic wave mode, and when the frequency is much smaller than the buoyancy frequency, the fluid can be considered incompressible, and the AGWs tend towards internal GWs mode. The term “acoustic-gravity waves” is usually used when restoring forces due to both gravity and compressibility are important. AGWs are known to play a significant role in the coupling between the atmosphere/ionosphere and the ocean (Press and Harkrider, 1962; Harkrider and Press, 1967; Donn and Balachandran, 1981; Azeem et al., 2017). Atmospheric pressure waves are mechanical waves that are related to the density of the atmosphere. Compression and expansion are the high-pressure and low-pressure regions of motion in a medium.

The 2022 HTHH volcano eruption triggered tsunamis that affected the whole world (Carvajal et al., 2022; Ghent et al., 2022). ~~Conventional Tsunamis~~ tsunamis are typically generated by localized sea surface displacements caused by sources such as earthquakes and volcanoes, similar to the tsunamis directly induced by the 2022 Tonga volcano eruption (TITVE). Another tsunami is induced by the atmospheric pressure wave (TIAPW) ~~significant mechanism that occurred was the atmospheric pressure wave that excited the~~ ~~tsunamis~~ (Kubota et al., 2022; Gusman et al., 2022). Tsunami can generate upward propagating AGWs through water-air interface and propagate to ~~the height of~~ the thermosphere/ionosphere (Hines, 1972; Peltier and Hines, 1976; ~~Pradipta et al., 2023;~~

Hickey et al., 2009, 2010; Occhipinti et al., 2013; Vadas et al., 2015; Laughman et al., 2016; Nishikawa et al., 2023; Pradipta et al., 2023). Using the red line airglow imager, Makela et al. (2011) detected airglow disturbance in Hawaii that arrived 1hr earlier before of the tsunami generated by the 11 March 2011 Tohoku earthquake. Also using the redline airglow, Smith et al. (2015) observed tsunami sea-wave and GW almost simultaneously in Chile. Inchin et al. (2020) used a three dimensional (3D)-numerical model to simulate the atmospheric AGWs generated by tsunami. They found that bathymetry variations significantly affected the tsunamis and the AGWs excited by tsunamis, leading to their nonlinear evolution process. More recently, Inchin et al. (2022) ~~simulated the modulation of tsunami induced AGWs on the mesopause airglow radiation~~ performed the numerical simulations of mesopause airglow radiation fluctuations induced by tsunami-generated AGWs, and found that large-scale tsunamis can cause detectable and quantitative disturbances of mesopause airglow through AGWs.

As far as we know, the research on the impact of tsunamis induced atmospheric AGWs on the atmosphere and ionosphere shown above is all caused by conventional tsunami. There are only two rare studies on the ground-based airglow observations of AGWs caused by this ~~conventional~~typical-type tsunami, and both are limited to red line observations (Makela et al., 2011; Smith et al., 2015). However, the observation of tsunami induced AGWs in the mesopause region observed by ground-based airglow imaging has never been reported. ~~Neither has AGWs originate from tsunamis induced by the atmospheric pressure wave (TIAPW) been studied.~~ In this study, we first reported the propagation characteristics of the AGWs generated by the tsunamis triggered by the 2022

HTHH volcano eruptions in the mesopause region using the ground-based airglow imager observation network. We then focus on the coupling process of atmospheric pressure waves triggering tsunamis, and then tsunamis generating atmospheric AGWs through air-water-air-coupling process (~~air-water-air-coupling-process~~) in the far-field area of the 2022 HTHH volcano eruption.

2. Data and Methods

2.1 ~~Multi Double~~ layer airglow imager network

A multi-layer airglow observation network (Xu et al., 2021) was built to study atmospheric disturbances excited by severe weather events, such as thunderstorms (Xu et al., 2015), typhoons (Li et al., 2022) and volcanic activities. Figure 1 shows the distribution of the multi-layer airglow observation network station. The multi-layer airglow observation network mainly includes the OH airglow network, which has been used to observe the airglow layer at the height of 87 km; the OI airglow network has been used to observe the airglow layer at the height of 250 km. In addition, there were 557 nm airglow and Na airglow imagers installed at some stations, such as Xinglong Station (40.4°N, 117.6°E). The airglow network can provide observation with high temporal and spatial resolution. The temporal resolution is 1 min and the spatial resolution is 1 km. The time resolution of OH and 557 nm airglow imager is 1 minute, while the resolution of OI airglow is 2 minutes. The spatial resolution of the airglow imager at the airglow layer is not uniform. The resolutions of OH, OI 557 nm, and OI 630 nm airglow in the zenith direction are 0.27 km, 0.29 km, and 0.77 km, respectively, while in the zenith angle of 60°, the resolutions are 1.01 km (OH), 1.11 km (OI 557 nm), and 2.65 km (OI 630 nm), respectively.

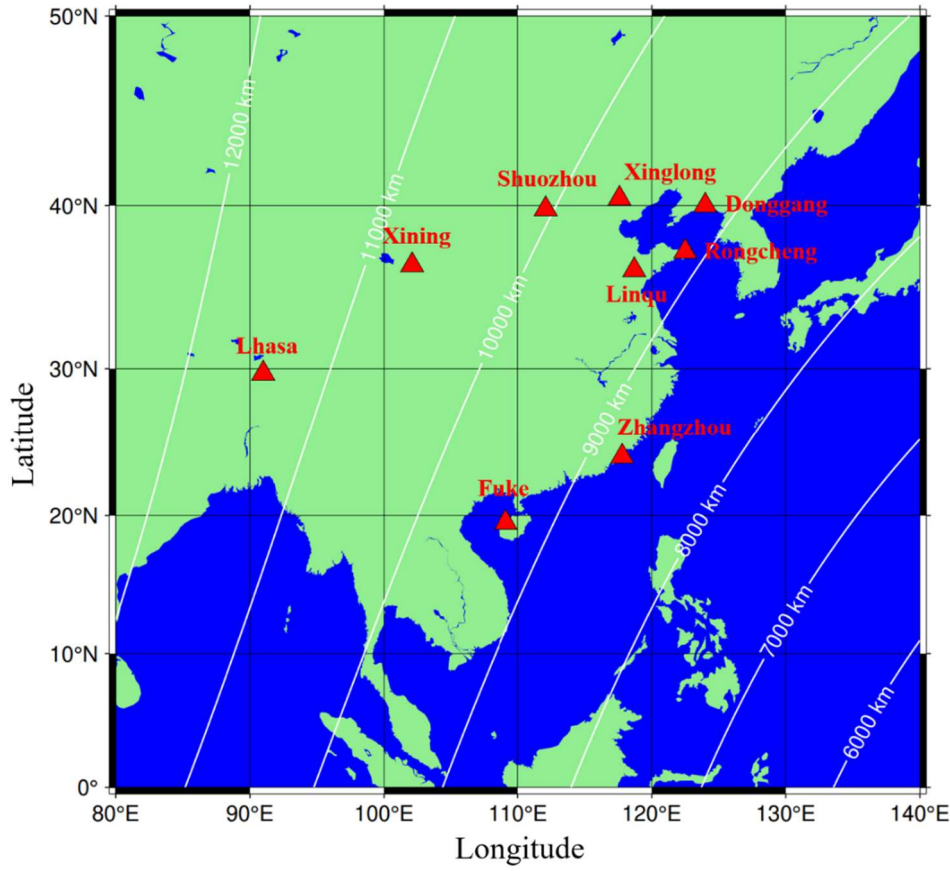


Figure 1 The distribution of airglow network stations, along with the large circular centered on the Tonga volcano and its radius length, is also marked in the figure

2.2 Spectral analysis of atmospheric wave parameters

The airglow image was calibrated with the help of standard star map (Garcia et al., 1997) and projected into geospatial space. The background radiation is removed by time differential (TD) method (Swenson and Mende, 1994), to highlight atmospheric fluctuations. The atmospheric wave parameters (horizontal wavelength λ_h , observed horizontal phase speed c , and the relative intensity perturbation I'/I) are extracted from spectral analysis method. Figure 2c presents the two-dimensional cross spectrum obtained from Fig. 2a and 2b. Zonal (k_x) and meridional (k_y) wave numbers are determined from the peak position of the spectra. The horizontal wavelengths λ_h are obtained from the

expression of $\lambda_h = 2\pi / \sqrt{k_x^2 + k_y^2}$. The observed speeds c are calculated from the phase (φ) (Fig. 2d) at the maximum peak of the cross spectrum as $c = \frac{\varphi}{2\pi} \frac{\lambda_h}{\Delta t}$, where Δt is the time interval between the two TD images. The amplitudes of intensity perturbations were calculated by integrating the power surrounding the central peaks of the power spectrum. To eliminate noise, the energy of the wave spectrum should be greater than 10% of the total spectrum (Tang et al., 2005).

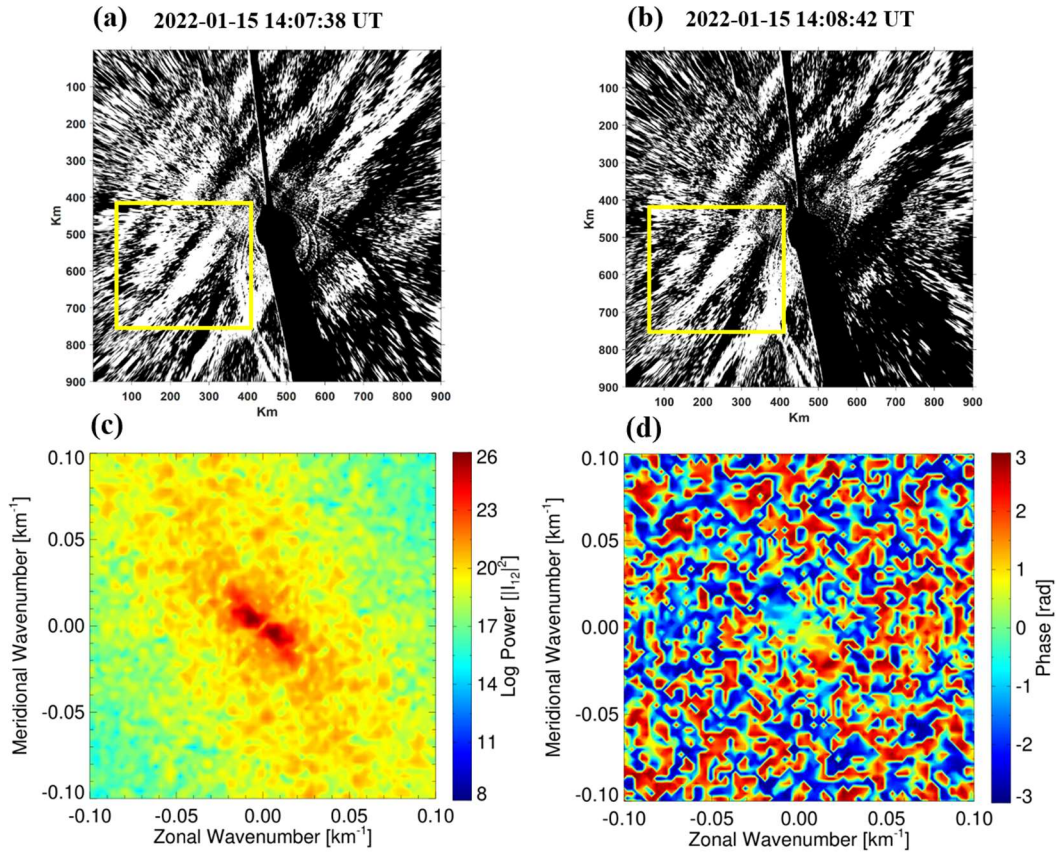


Figure 2 The time difference images (a-b) obtained from the Xinglong OH airglow imager on the night of 15 February 2022. Each image is projected on an area of 250 km × 250 km. The (c) cross spectrum and (d) phase of the time difference images from a and b using 2-D fast Fourier transform.

2.2.3 Tsunami simulation model

Tonga submarine volcano erupted on 15 January 2022, and generated tsunamis that were detected around the globe, affected particularly the Pacific region. In this study, two

types of tsunamis were simulated, conventional tsunami simulations and atmospheric pressure wave-induced tsunami simulations. The linear-shallow water equations in the spherical coordinate system are used to simulate the tsunamis from the localized source and atmospheric pressure wave. The continuity equation of a linear shallow water wave model in spherical coordinates is:

$$\frac{\partial \eta}{\partial t} + \frac{1}{R \sin \theta} \left[\frac{\partial (ud)}{\partial \varphi} + \sin \theta \frac{\partial (vd)}{\partial \theta} \right] = 0 \quad (1)$$

where η is free surface elevation (m), d is the water depth (m), R is the Earth's radius (6371,000 m), φ is longitude, θ is colatitude.

While the momentum equations of the linear shallow water wave model are:

$$\frac{\partial u}{\partial t} + \frac{1}{R \sin \theta} \left[g \frac{\partial \eta}{\partial \varphi} + \frac{1}{\rho} \frac{\partial p}{\partial \varphi} \right] + fv = 0 \quad (2)$$

$$\frac{\partial v}{\partial t} + \frac{1}{R} \left[g \frac{\partial \eta}{\partial \theta} + \frac{1}{\rho} \frac{\partial p}{\partial \theta} \right] - fu = 0 \quad (3)$$

where, u is the velocity along the lines of longitude (m/s), v is the velocity along the lines of latitude, g is the gravitational acceleration (9.81 m/s^2), p is the atmospheric pressure (Pa), ρ is the sea water density (1026 kg/m^3), f is the Coriolis coefficient. For the atmospheric pressure wave-induced tsunami simulation, the moving change pressure terms as an input to tsunami simulation momentum equation. The atmospheric pressure wave model is based on the Equation (1) in Gusman et al. (2022).

For the tsunami simulations from a localized source, a B-spline function (Koketsu and Higashi, 1992) below is used to represent the circular water uplift source at the volcano:

$$f(x, y) = \sum_{i=0}^3 \sum_{j=0}^3 c_{k+i, l+j} B_{4-i} \left(\frac{x-x_k}{h} \right) B_{4-j} \left(\frac{y-y_l}{h} \right) \quad (4)$$

$$\text{where } B_i(r) = \begin{cases} r^3/6, & i = 1 \\ (-3r^3 + 3r^2 + 3r + 1)/6, & i = 2 \\ (3r^3 - 6r^2 + 4)/6, & i = 3 \\ (-r^3 + 3r^2 - 3r + 1)/6, & i = 4 \end{cases} \quad (5)$$

x_k and x_l stand for the coordinates of the knots along the x and y axes, h is the characteristic diameter of water uplift, r is the great-circle distance from the volcano eruption center, $c_{1,1} = 1$ and the other $c_{k+i,l+j} = 0$. In this study, the modelling domain covers the Pacific Ocean and some parts of Indian Ocean and the Caribbean with a grid size of 5 arc-min. For detailed tsunami simulation algorithms, please refer to Gusman et al. (2022).

The models for the 2022 HTHH volcanic eruption used in this study was estimated and validated with observations at offshore DART stations around the Pacific Ocean in a previous study (Fig. 3 and Fig. 7 of Gusman et al., 2022).

2.3.4 Ray tracing method

The following ray tracing equations (Lighthill, 1978) describes the propagation path of AGWs.

$$\frac{dx_i}{dt} = \frac{\partial \omega}{\partial k_i} = c_{g_i} \quad (16)$$

$$\frac{dk_i}{dt} = -\frac{\partial \omega}{\partial x_i} \quad (27)$$

where x_i , k_i , c_{g_i} ($i=1, 2, 3$), and ω are the position vector, wavenumber vector, group speed, and intrinsic frequency, respectively.

~~There is no real-time temperature data available in this study.~~ Using the dispersion relation of acoustic gravity wave (Yeh and Liu, 1974), we can assess the vertical propagation state of AGWs. The dispersion relation is as follows

$$m^2 = \frac{\omega^2}{c_s^2} \left(1 - \frac{\omega_a^2}{\omega^2}\right) - k^2 \left(1 - \frac{\omega_b^2}{\omega^2}\right) \quad (38)$$

where m is the vertical wave number, k is the horizontal wave number, c_s the local speed of sound, $\omega = k(c - u)$ is intrinsic frequency, ~~c is the horizontal phase speed,~~ u is the background wind speed in the direction of wave propagation from [meteor radar observations and ERA-5 \(Hersbach et al., 2020\)](#). $\omega_a^2 = \frac{g}{T} \frac{dT}{dz} + \frac{\gamma g}{4H}$ is acoustic cutoff frequency, $\omega_b^2 = \frac{g}{T} \frac{dT}{dz} + \frac{(\gamma - 1)g}{\gamma H}$ is buoyancy frequency, g is the gravitational acceleration, and T is temperature from [the Sounding of the Atmosphere using Broad band Emission Radiometry \(SABER\) instrument on the Thermosphere Ionosphere Mesosphere Energetics and Dynamics \(TIMED\) satellite](#). When $\omega > \omega_a$ or $\omega < \omega_b$, $m^2 > 0$, AGW can propagate freely, while when $\omega_b < \omega < \omega_a$, $m^2 < 0$, the wave is evanescent.

3. Results and Discussion

3.1 Upper Atmospheric Airglow Responses to HTHH Volcanic Eruption via Lamb Waves

Five groups of atmospheric waves (wave packets #1-5) were observed in the mesopause region by the ground-based airglow network. [Refer to this Supplement \(https://doi.org/10.5446/66190\) for detailed wave propagation status. To eliminate random disturbances, we also made videos of two days before and after the volcanic eruption \(https://av.tib.eu/series/1689\). From the videos, it can be seen that the OH airglow layer was very calm during this period.](#) Figure 4-3 shows the wave packet #1 observed [by the airglow imager network at each station of the OH airglow network](#) (top panels). Wave packet #1 entered the view of the ~~OH~~ airglow network approximately 8 hr after the HTHH volcanic eruption [\(Left image of top panels\)](#). Three hours after wave packet #1 entered the

214 field of view, wave packet #2 was observed by the ~~OH~~-airglow network. The leading front
215 of wave packet #2 has an uninterrupted continuous front, which almost covers the whole
216 Chinese Mainland (middle panels). Interestingly, we observed AGWs accompanying wave
217 packet #2 (hereafter wave packet #3) over the northwest region of the Yellow Sea (~~Middle~~
218 Left image of middle panels). Wave packet #2 always keeps a stable state in the process of
219 propagation, and maintains a regular front when propagating over Lhasa Station (29.7°N,
220 91.0°E). Wave packet #4 exhibits strong instability characteristics during propagation.
221 Compared to the continuous leading front of wave packet #2, the fronts of wave packets #4
222 and #5 are separated (bottom panels). We also found that wave packet #5 (~~Left image of~~
223 ~~bottom panels~~) propagate more than 3000 km inland (propagating to the area west of
224 longitude 90°E).

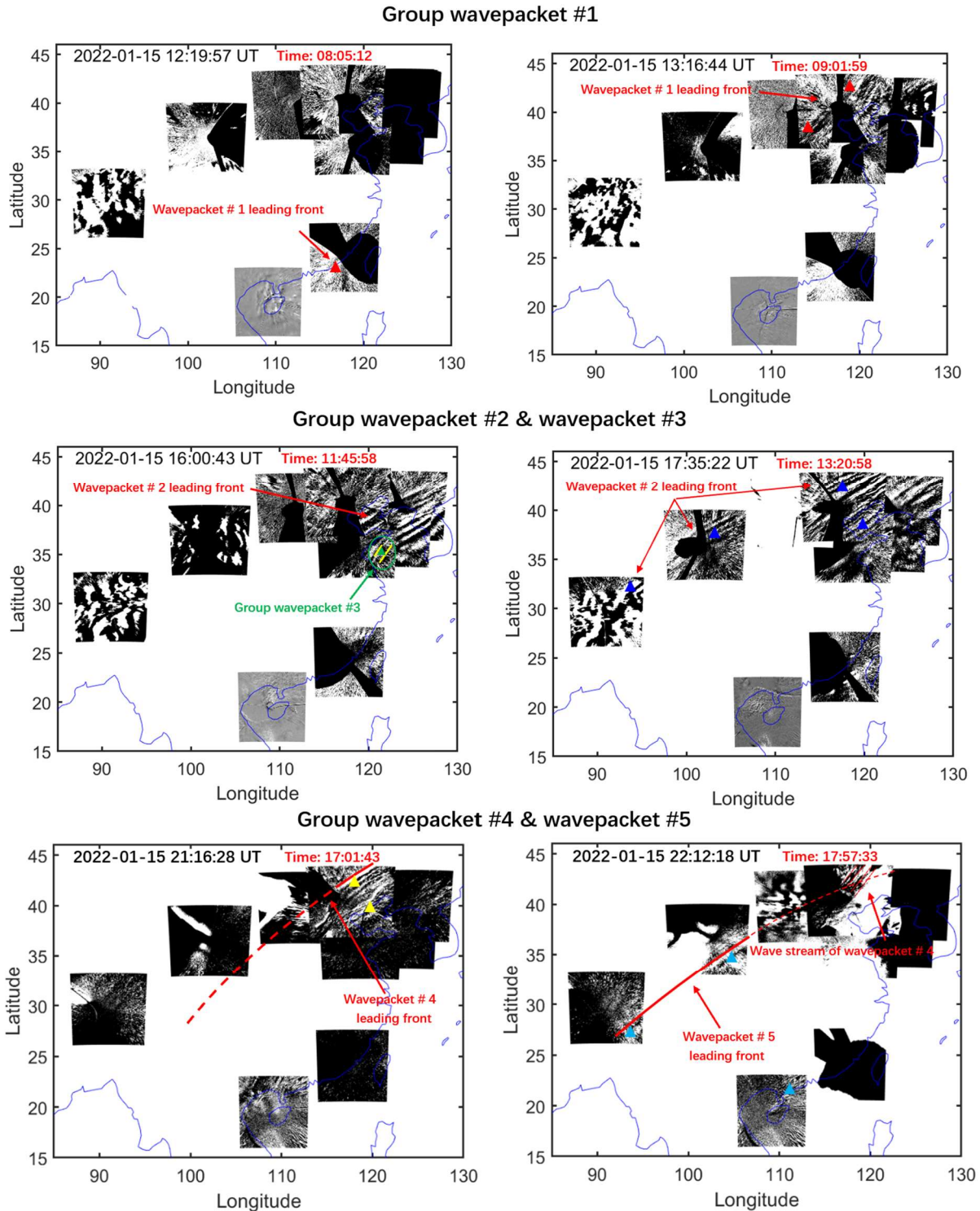


Figure 1-3 Five strong group atmospheric waves associated with the Tonga volcano eruptions were observed in the mesopause region by the ground-based airglow network. Different colored triangles correspond to each wave event sampling point, while red, blue, green, yellow, and cyan correspond to wavepackets #1, #2, #3, #4, and #5, respectively. The red time markers in this figure and the following figure represent the lapse time since the volcano eruption.

Figure 2-4 shows the distribution of wave parameters for multi-group of atmospheric

232 waves (wave packets #1-#5) from cross spectral analysis. relationship between horizontal
233 phases speed and relative amplitude and longitude. The phase speed of wave packet #1 is
234 approximately ~~312~~ 309 m/s. Wave packet #2 displays a slightly slower phase speed, with
235 average phase speed of ~~238~~ 236 m/s. The horizontal phase velocity speeds of group wave
236 packets # ~~43~~-5 ~~is less than that of the first GW, which is~~ are mainly distributed in the range
237 of 200 m/s to 215 m/s approximately 207 m/s., which is smaller than that of wave packets
238 # 1-2. The horizontal wavelengths of these five group wave packets are mainly distributed
239 in 80 km-105 km, while the observation periods are relatively small and mainly
240 concentrated in 5.7 min-7.2 min. For amplitude, the average amplitude of the lamb wave
241 L1 mode (5.4%) is higher than that of the lamb wave L0 mode (3.2%). Wavepackets # 3, #
242 4, and # 5 have relatively small amplitudes, mainly distributed between 0.85% and 1.25%.

243 ~~For wave amplitude, the relative amplitude of wave packet #2 is greater than that of~~
244 ~~wave packets #1 and # 4-5, with a maximum amplitude of nearly 30%, and wave packet~~
245 ~~#4-5 has the smallest relative amplitude.~~

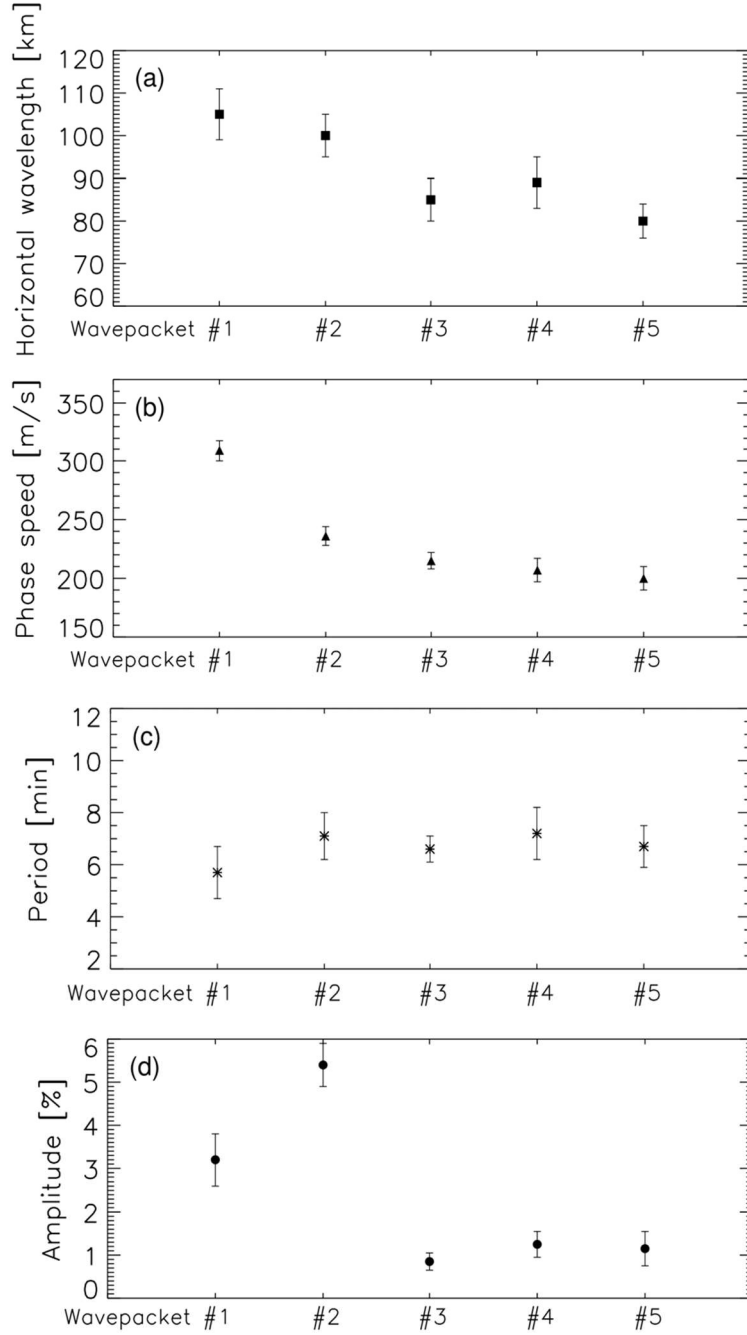


Figure 2-4 Distribution of (a) horizontal wave wavelength, (b) phase speed, (c) period, and (d) amplitude parameters for multi-group of atmospheric waves (wave packets #1-#5). The calculation of wave packet parameters comes from the average value of the wave passing through the sampling points in Fig 3.

The HTHH volcano eruption produced Lamb waves that propagate around the globe⁴, (Wright et al., 2022) causing sudden changes in surface pressure (Omira et al, 2022; Takahashi et al., 2023). Figure 3 shows vertical distribution characteristics of atmospheric

~~waves caused by Tonga volcano eruption from the surface to the thermosphere atmosphere.~~

Figure ~~3d~~ 5f shows the surface air pressure data of Xinglong station (40.4°N, 117.6 °E). At

13:15 UT on January 15, 2022, the air pressure dropped sharply from 920 Pa to 917.7 Pa,

indicating that Lamb wave arrived at the surface of Xinglong station at 13:15 UT. A small

disturbance of air pressure occurs at 16:33 UT. Figures 5e and 5d present Himawari-8

6.2 μ m brightness temperature at 13:10:00 UT (Otsuka, 2022). It can be seen that the

leading front of Lamb wave L0 mode happens to pass through the zenith direction of

Xinglong station. The time when wave packet #1 (Fig. ~~3b~~ 5b) and wave packet #2 (Fig.

~~3e~~ 5c) reach the zenith direction of Xinglong Station from OH airglow observation is

13:13:34 UT and 16:32:16 UT, which matches the time for surface pressure disturbances

quite well. The phase speed of the wave packet #1 (~~~312~~ 309 m/s) is very close to the speed

of surface Lamb wave (L0 mode). From the Fig 5, it can be seen that the phase of the lamb

wave L0 mode is almost vertical from the ground to the stratosphere and then to the

mesosphere. The wave packet # 2 with a slower phase speed (~~~238~~ 236 m/s) is consistent

with the Lamb wave L1 mode in theoretical predictions (Francis, 1973) and simulations

from WACCM-X model (Liu et al., 2023). However, at almost the same time, the wave

front observed in the thermosphere (Video Supplement, <https://doi.org/10.5446/66280>)

with a slightly faster phase speed of 342 m/s is nearly 550 km a head of the wave front in

the mesopause region in the horizontal propagation direction and ahead of time

approximately 30 min (Fig. ~~3a~~ 5a). This is in good agreement with theoretical and modeling

results (Fig. 4 of Lindzen and Blake, 1972; Fig. 2 of Liu et al. 2023), which show that the

wave fronts of Lamb wave ~~L0~~ below the lower thermosphere are vertical and tilt forward

above. As for Lamb wave L1 mode, the ground and mesopause region provide waveguide surfaces, resulting in maximum wave energy between the two layer, while the phase does not change with height (Francis, 1973).

As for why the observed Lamb wave L0 shape in the OH airglow layer is not a strong leading wave with much weaker trailing waves, it may be caused by the following factors. It is seen from model simulations that the wave amplitudes of L0 and L1 modes are not uniform at the wave front. This non-uniformity becomes more pronounced in the upper atmosphere (e.g. Fig 2 of Liu et al., 2023), probably as a result of the large variation of the background atmosphere propagation conditions. It is thus possible that over certain regions the trailing waves become comparable with the leading wave. In addition, due to the smaller field of view of the airglow imager compared to satellite observations, some structures may be related to local fine structures, especially in the middle and upper layers where many internal waves have significant amplitudes, which may be relatively more significant than Lamb waves.

As mentioned above, the amplitude of Lamb wave L1 mode in the mesopause region is greater than that of L0 mode, which may be due to the fact that L1 mode is an internal wave below the mesopause (Liu et al. 2023). For an isothermal atmosphere, the Lamb wave L0 mode amplitude grows with altitude z as $e^{\kappa z/H}$, where H is the scale height, $\kappa = (\gamma - 1)/\gamma$, and γ is the ratio of specific heats (~ 1.4). However, the amplitude of internal GWs varies as $e^{z/2H}$. The amplitude of internal waves increases with height at a rate greater than that of surface modes.

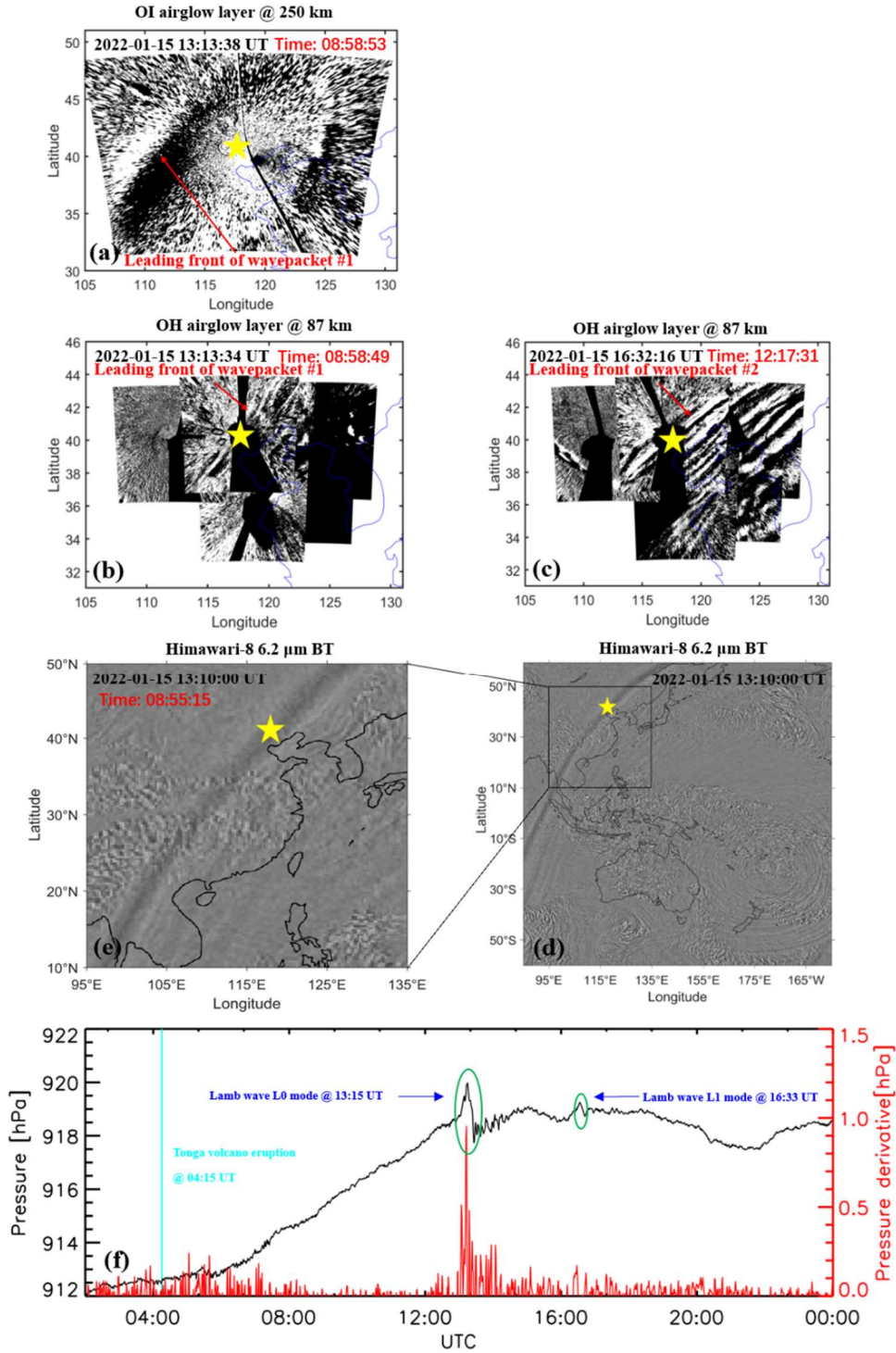


Figure 3-5 (a) OI 630 nm airglow observation at 13:13:18 UT. OH airglow network observations when (b) wave packet #1 and (c) wave packet #2 pass through the zenith direction of Xinglong Station at 13:13:34 UT and at 16:32:16 UT, respectively. (d)-(e) Himawari-8 6.2 μm brightness temperature at 13:10:00 UT. (df) The surface time series of surface pressure pressure profile obtained from Xinglong observation station. The red line represents the time derivative of the pressure. The sudden change of air pressure at 13:15 UT indicates the arrival time of Lamb wave L0. A small disturbance of air pressure occurs at 16:33 UT indicates the arrival time of Lamb wave L1. The yellow stars represent the location position of the Xinglong station.

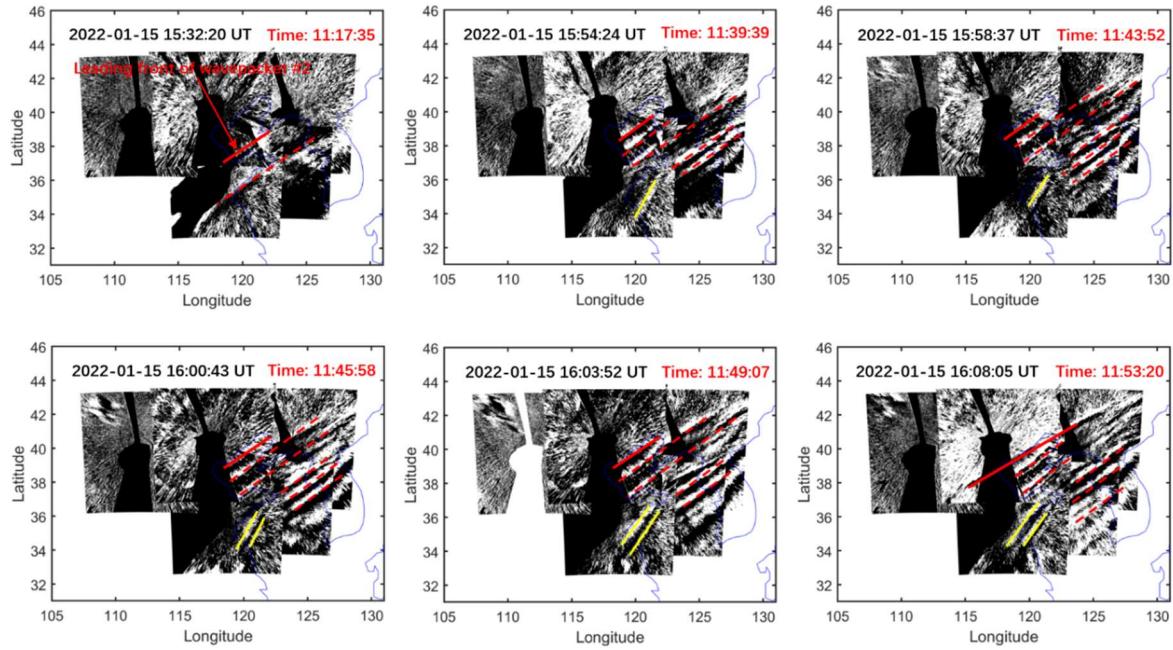


Figure 4-6 The red solid lines indicate leading wave front of the wave packet #2. The yellow solid lines marks wave packet #3 other wave fronts, which are clearly not parallel to the wave fronts of wave packet #2.

Figure 4-6 shows the time sequence of propagation image of wave packet #3. We found that with the propagation of wave packet #2, there is an AGW (wave packet #3) with a certain angle between its phase plane (yellow solid line) and the phase plane of wave packet #2. This implies that the source of the wave packet #3 is different from that of wave packet #2. The horizontal wavelength of the wave packet #3 near the coast is $84 \text{ km} \pm 5 \text{ km}$.

~~We find the horizontal wavelengths of the atmospheric AGW observed by airglow network are very consistent with the simulated tsunamis near the coast.~~

3.2 Simulation of Tsunami induced by HTHH Volcano Eruption

The 2022 HTHH volcano eruption triggered global atmospheric pressure waves. The simulated atmospheric pressure waves propagate at an approximate constant speed of 317 m/s, and the amplitude decreases with the distance from the volcano (Gusman et al., 2022).

Figure 5–7 shows snapshots of the TIAPW and TITVE simulation results. The leading TIAPW excited by the pressure disturbances travels at the same speed as the atmospheric pressure wave and is followed by subsequent sea waves generated earlier in the atmospheric pressure wave propagation which thereafter travel at the conventional tsunami propagation speed. Under a given pressure gradient, the discharge flux in deep sea is much greater than that in shallow water. A deep bathymetric feature such as the Kermadec Tonga Trench can more effectively generate tsunami waves. The wave train following the leading wave travelling over the trench appear to be larger than those travelling in other directions.

The propagation speed of TITVE from the shallow water (long) wave approximation is $v = \sqrt{gH_0}$ (Salmon, 2014), where g is the gravitational acceleration and H_0 is the ocean depth. For sea water with a general depth of 4 km, the speed of shallow water wave is about 200 m/s. Therefore, the TIAPW is significantly faster than the TITVE. The amplitude of TITVE is greater than that of tsunamis generated by atmospheric pressure waves. The wave train following the leading wave of TITVE exhibit finer structures with scales smaller than that of TIAPW. We found that the TIAPW arrived along the coast of Chinese Mainland about 4-5 hours earlier than the TITVE. However, in the relatively shallow Yellow Sea, the leading TIAPW is very small and only the later waves of the TIAPW are relatively large.

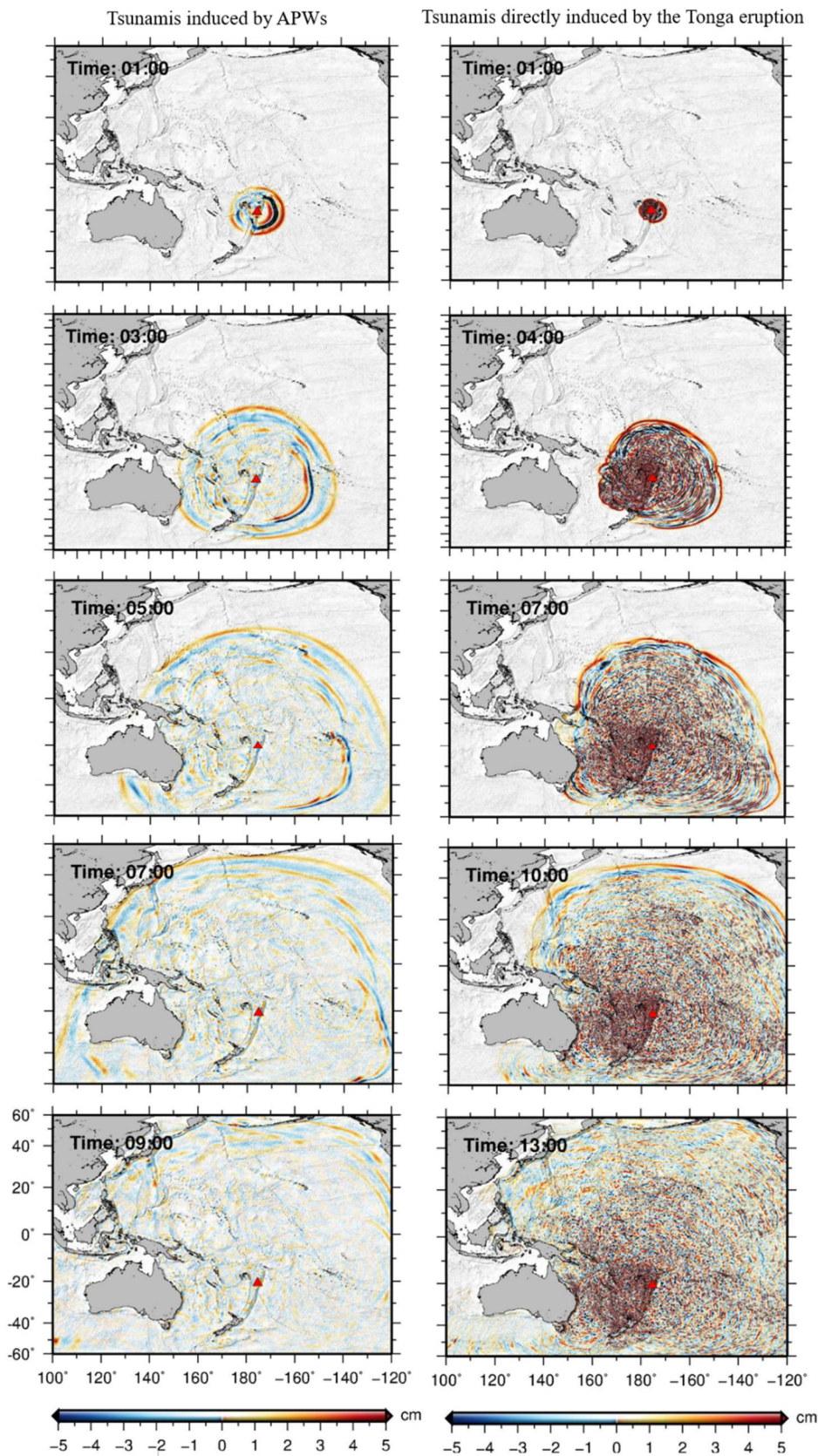


Figure 5-7 Snapshots of simulated tsunamis induced by the atmospheric pressure wave (left panels) and tsunamis directly induced by the Tonga volcano eruption (right panels).

3.3 Upper atmosphere responses to HTHH volcanic eruption via Air-Sea Interaction

Figure 6-8 shows the simulation results of TIAPW and TITVE near the coast of Chinese Mainland 11 hr (15:15 UT) and 15 hr (19:15 UT) after the volcanic eruption, respectively. Air pressure waves are not very efficient at directly exciting tsunamis in shallow water due to the weaker air-sea coupling (Gusman et al., 2022; Yamada et al., 2022). The Yellow sea is quite shallow, so the amplitude of the leading of TIAPW is very small there. The leading wave is followed by subsequent waves with larger amplitudes, which propagate in the same direction as the leading wave but at the conventional tsunami speed (Gusman et al., 2022). We found that the TIAPW and TITVE on the continental shelf have shorter wavelengths compared with those in the deep ocean. When the tsunamis approached the coast of China, three groups of AGWs (wave packet #3 and wave packets #4-5) were observed by the airglow network. The time when the AGW entered the view of the airglow network was very close to the time when the Tonga tsunamis reached the coast of Chinese Mainland. The wave packet #3 entered the airglow network at 15:30 UT and the wave packets #4-5 entered the airglow network at 19:40 UT. This strongly suggests that the wave packets detected by the airglow network are correlated to the tsunamis near the coast. We found that as the tsunamis approached the coast of China, they diffracted between Taiwan and Philippines and became discontinuous. And the wave packets #4 and #5 we observed was also discontinuous, which further confirms the correlation between wave packets # 4-5 and discontinuous tsunamis. We estimate that the average wavelength of TIAPW near the coast of the Yellow Sea is approximately $82 \text{ km} \pm 4 \text{ km}$, which is very consistent with the horizontal

wavelengths of the atmospheric AGW observed by airglow network as mention above
 (84 km \pm 5 km), while the average wavelengths of TITVE near the coast of the Yellow
 Sea and South Sea are 95 \pm 5 km and 86 \pm 5 km, respectively.

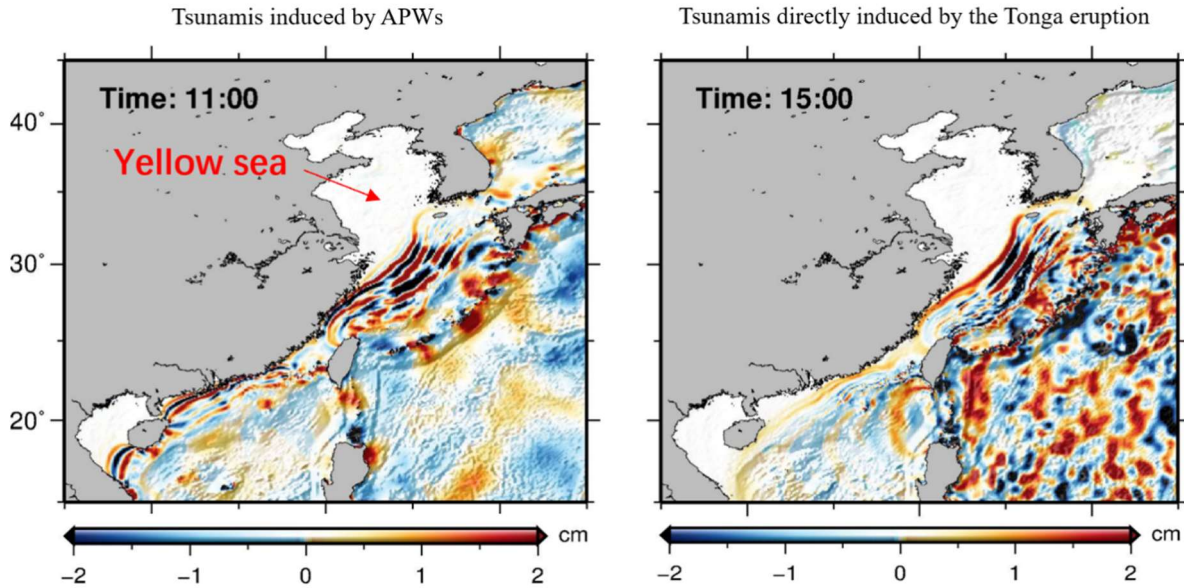


Figure 6-8 Simulated tsunamis induced by the atmospheric pressure wave (left panels) and tsunamis directly induced by the Tonga volcano eruption (right panels) near the coast of Chinese Mainland. The marked time represents the time after the volcanic eruption.

Figure 9a shows three TIMED satellite tracks with descending track #1 along the coast of China, ascending track #1 located east of the Korean Peninsula, and ascending track #2 inland China. Figure 7b-9b shows the square of vertical wave number m^2 profile (black) derived from the average temperature from the limb viewing of the Sounding of the Atmosphere using SABER/ TIMED measurement locations marked by the red circles and triangles in Fig.7a9a. We take the average temperature of ascending track #1 and descending track #1 serves as the background temperature for the wave packet #3 and ascending track #1 as the background temperature of the wave packets #3-4-5 when they propagate in the coastal vicinity. We take ascending track #2 as the background temperature

of wave packets #3-4-5 when they propagate inland China. and HWM-14. The peak height of OH airglow layer is 87 km. We found that the propagation of wave packet #3 (dash-dotted line) is in a state of free propagation in the coastal vicinity.

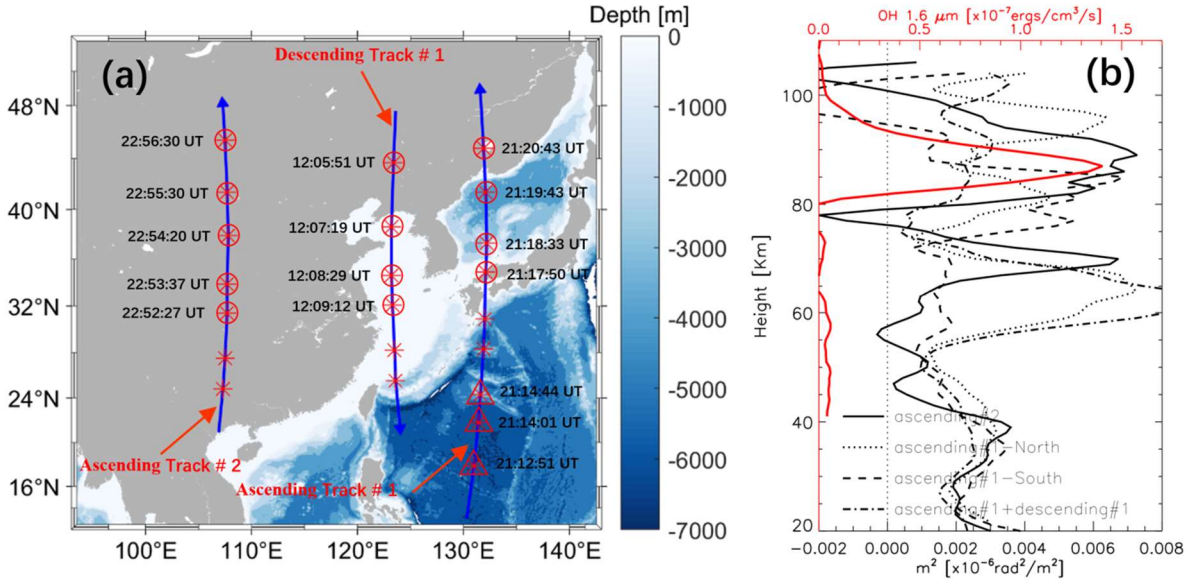


Figure 7-9 (a) Ascending and descending SABER/TIMED satellite tracks over Chinese Mainland. Background representative ocean depth map. (b) Square of vertical wave number m^2 profiles: black solid line profile derived from the ascending track #2 (marked by the red circle), dotted line profile derived from the ascending track #1-North (marked by the red circle), dashed line profile derived from the ascending track #1-South (marked by the red triangle), and dash-dotted line profile derived from the average the ascending track #1 and descending track #1 (marked by the red circle) from the SABER/TIMED measurement locations in (a). The red line represents the OH 1.6 μm emission intensity obtained by the SABER/TIMED.

Figure 10 show the background field used for ray tracing analysis for the TIAPW event. The temperature comes from TIMED/SABER and ERA-5 and wind data from meteor radar and ERA-5. Meteor radar wind field is from Beijing station (40.3°N, 116.2°E). Figure 11 shows the results of ray tracing for the wave packet #3. We find that the source location of AGWs over the coast of Chinese Mainland falls in the near coast where the tsunami occurred.

Tsunami simulation shows that the surface wave height along the coast of Chinese

Mainland is in the order of 2 cm. There have been theoretical (Peltier and Hines, 1976) and observational (Grave and Makela, 2015, 2017) studies on the relationship between the amplitude of tsunamis and GWs. Peltier and Hines (1976) found that a tsunami amplitude of ± 1 cm at sea level can cause vertical motion of ionospheric E layer and F layer ± 100 m. A more direct observational evidence is that Grawe and Makela (2017) provided airglow observation of tsunami-generated ionospheric signatures over Hawaii caused by the 16 September 2015 Illapel earthquake. They found that vertical disturbances on the sea surface not exceeding 2 cm (Fig. 3b of Grave and Makela, 2017) can create detectable signatures in the ionosphere (Fig. 1 of Grave and Makela, 2017). Therefore, we suggest that the waves with larger amplitudes following the leading of TIAPW interact with the atmosphere after arriving at the coast of Chinese Mainland to generate the upward propagating AGW packet.

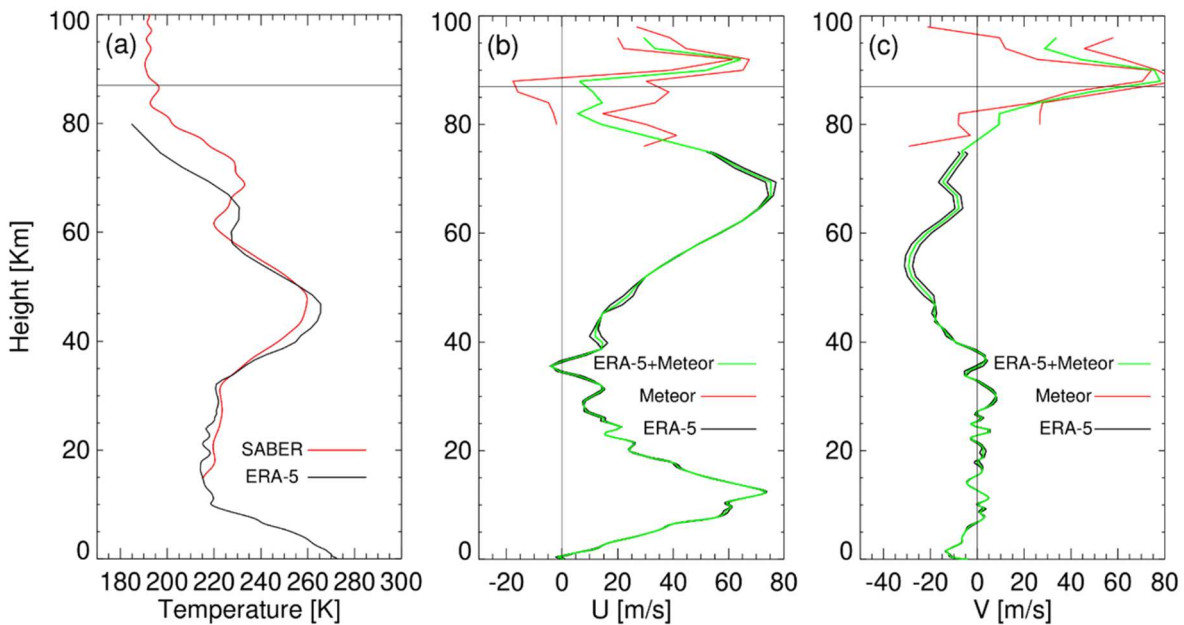


Figure 10 The background field used for ray tracing analysis for the TIAPW event (a) Saber temperature (red) comes from the average temperature of ascending track #1 and descending track #1 in Fig. 9, and ERA-5 temperature (black) comes from the average of 15:00 UT and 16:00 UT. (b) Meteor zonal wind field (red) and ERA-5 zonal wind field (black). (c) Meteor meridional wind field (red) and ERA-5 meridional wind field (black). The two red and black lines in (b) and (c) are respectively from

15:00 UT and 16:00 UT. The green lines represent the average of two lines. Meteor radar wind field is from Beijing station.

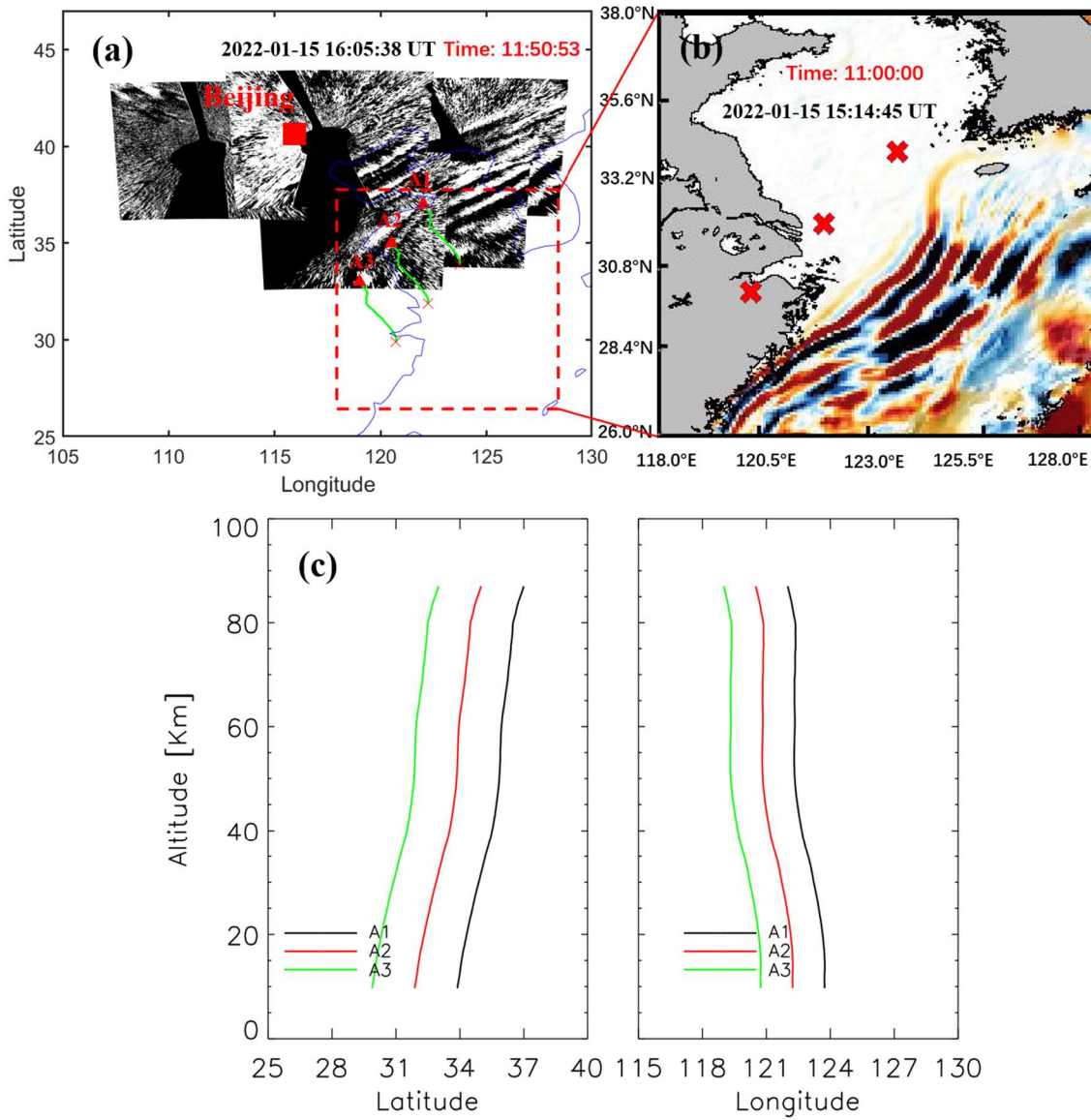


Figure 8-11 (a) Backward ray tracing results of the wave packet #3 observed by the OH airglow network. The red triangles and red crosses represent the trace start and termination points, respectively. (b) Simulated tsunamis induced by the atmospheric pressure wave (TIAPW) corresponding to the dotted rectangular area in (a). (c) Ray paths of the wave starting from the seven sampling points in (a).

According to the theory of AGW dispersion, the AGW propagating obliquely has the following approximate relationship: $\sin(\varphi) \sim T_B/T$, φ is the oblique propagation angle, T_B is the buoyancy period, T is the intrinsic period. Azeem et al. (2007) found that the disturbances in the ionosphere excited by the 2011 Tohoku tsunamis when they reached

the west coast of the United States. They concluded that the fluctuations observed in TEC satisfy AGW dispersion relation, and the period and horizontal wavelength of the TEC disturbances increased with distance from the West Coast of the U.S.

From the airglow network observations, we found that the wave packets #4-5 excited by the tsunamis, continues to propagate over the main land more than 3000 km from the coast. If the AGWs observed by the airglow network propagate freely rather than being constrained by duct satisfy the dispersion relation, we will obtain the propagation characteristics similar to that observed by Azeem et al. (2007) in the ionosphere from TEC observations. T_B is about 5min from the SABER/TIMED observation. The period of wave packet #3 is between 5.5 min and 8.5 min. The minimum propagation angle φ equals 35° , and the corresponding maximum propagation distance L is 125 km from $L \sim H_{oh}/\tan(\varphi)$ estimation, where $H_{oh}=87$ km is the height of OH airglow layer. However, our observation does not satisfy the free oblique propagation dispersion theory of AGWs. In addition, we did not find that the GW horizontal wavelength increased with the distance from the shore, as predicted by the theory of AGW oblique propagation. Therefore, the AGWs excited by the tsunami we observed in the mesopause region may be modulated by duct.

We did find a duct structure between 80 and 93 km (black solid line in Fig. 7b9b), while the wave packet #3 were in a state of free propagation when they propagate around the coastal vicinity of Chinese Mainland (dotted line and dashed line). The duct almost includes the whole OH airglow layer. Therefore, we believe that AGWs generated by TITVE may enter the duct in the process of propagation over Chinese Mainland. The duct structure over

Chinese Mainland can explain that the GWs generated by the tsunamis can propagate thousands of kilometers inland.

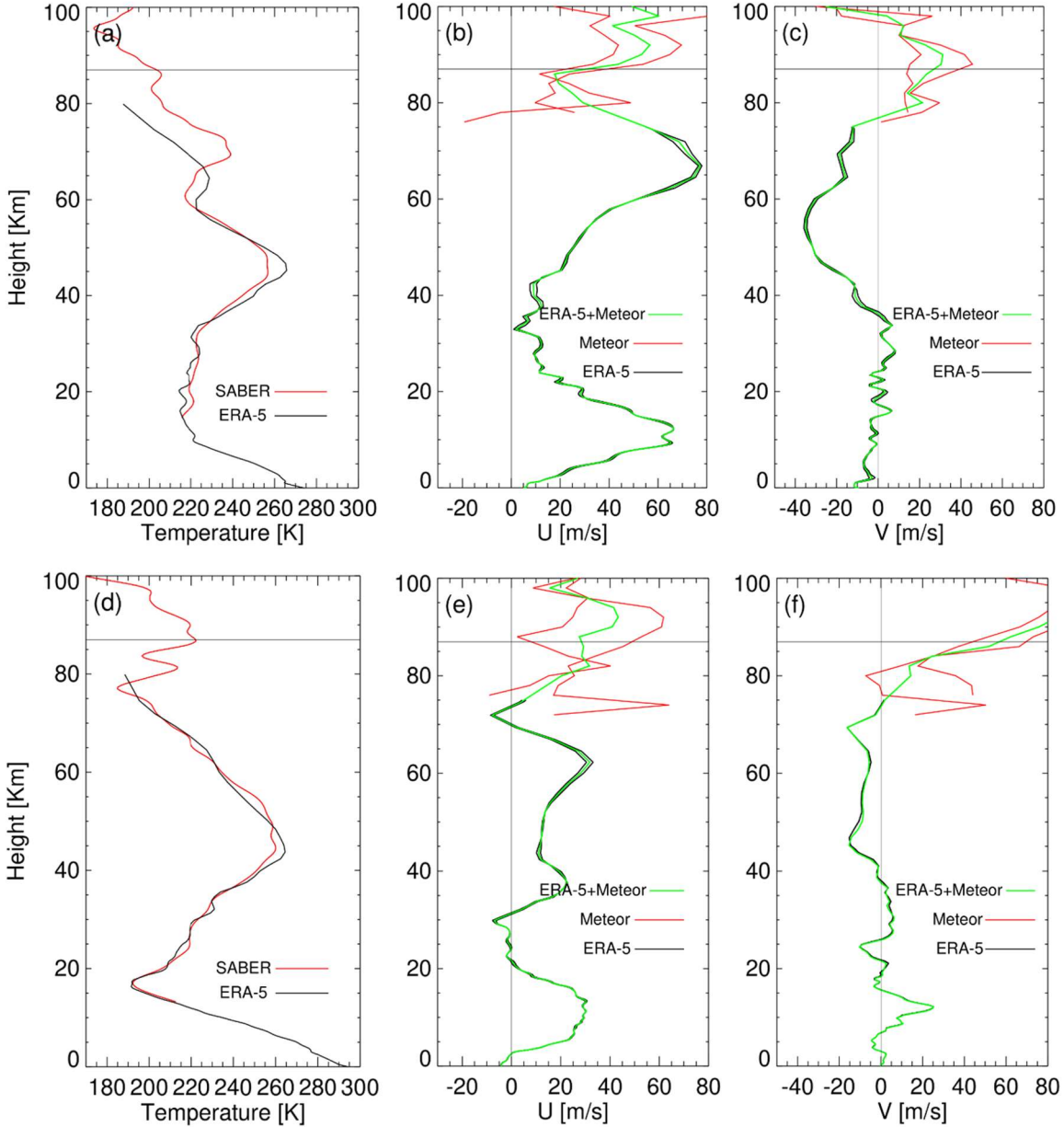


Figure 12 Similar for Figure 10, but for ray tracing analysis for the TITVE events. The SABER temperature field in (a) comes from ascending track #1(21:17:50 UT, 21:18:33UT, 21:19:43 UT, and 21:20:43 UT) in Fig. 9, and the meteor radar wind fields in (b) and (c) come from Beijing station. The SABER temperature field in (d) is from ascending track #1(21:12:51 UT, 21:14:01 UT, and 21:14:44 UT) in Fig. 9, and the meteor radar wind fields in (e) and (f) are from Ledong station.

Figure 9-13 shows the results of ray tracing for wave packets #4-5. The background field used for ray tracing analysis for the wave packets #4-5 is from Fig. 12. Meteor radar

wind field is from Ledong station (18.3°N, 109.4°E). The horizontal wavelength of wave packets #4 and #5 observed near the coast by the OH airglow network approximately 89 km \pm 6 km and 80 km \pm 4 km. We find that the source location of AGWs over the coast of Chinese Mainland falls in the near tsunami area, while the location of AGW ray termination over the inland (~~position B6 and B7 in Fig. 9d~~) is around 80 km (position B6 and B7 in Fig. 13d), which indicates that the wave meets the evanescent layer (Wrasse et al., 2006). This is consistent with the duct structure obtained through dispersion relation. Therefore, we suggest that TITVE interact with the atmosphere after arriving at the coast of Chinese Mainland to generate the upward propagating AGW packet. After reaching the mesopause region, this wave packet enters the wave duct structure in the horizontal propagation process, and this wave duct supports wave packet ~~#3-5~~ to propagate more than 3000 km inland China.

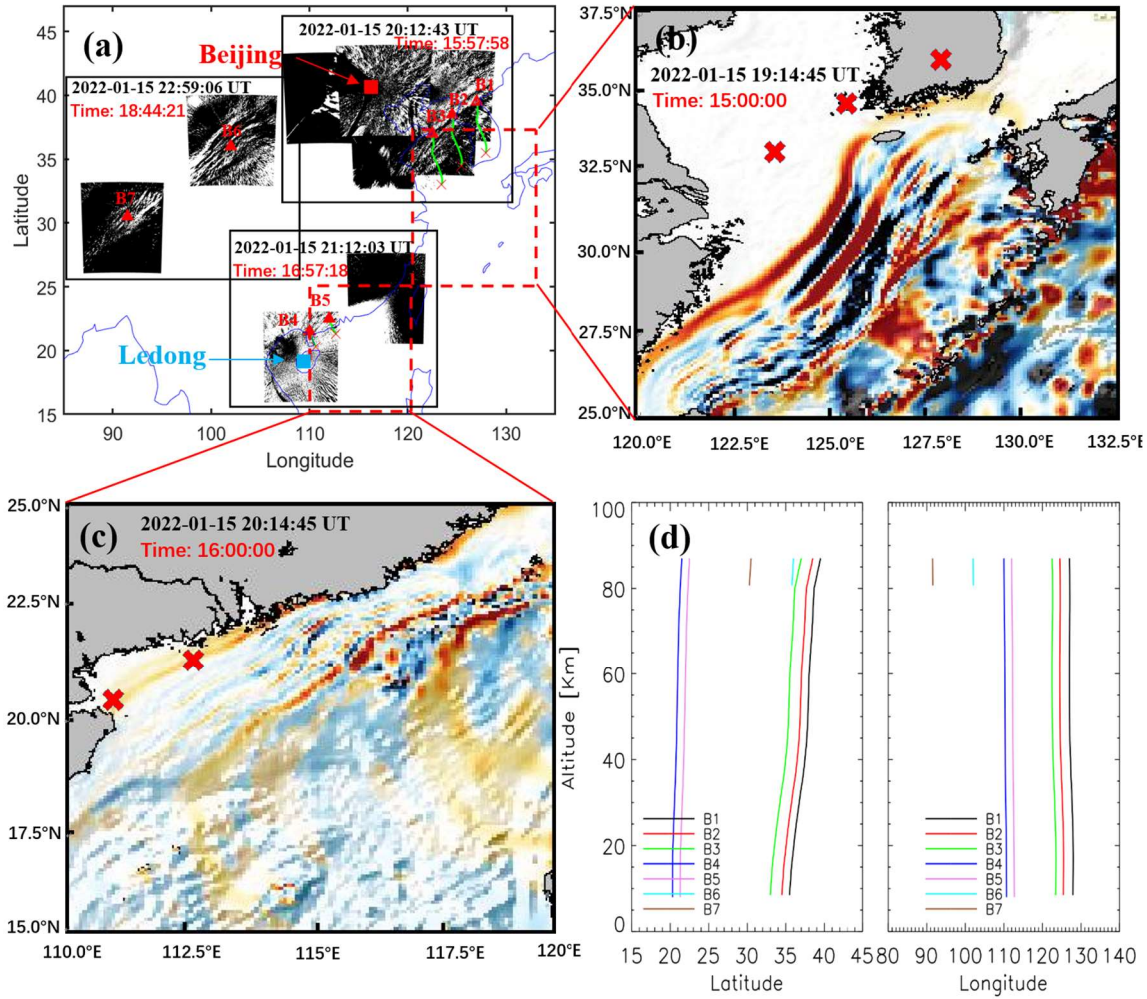


Figure 9-13 (a) Backward ray tracing results of the fourth and five group GWs observed by the OH airglow network. The red triangles and red crosses represent the trace start and termination points, respectively. (b) and (c) Simulated tsunami directly induced by the Tonga volcano eruption (~~TITVESWITVE~~) corresponding to the dotted rectangular area in (a). (c) Ray paths of the wave starting from the seven sampling points in (a).

4. Conclusions

Strong atmospheric disturbances, including Lamb waves, acoustic waves, and gravity waves, were triggered by the 2022 HTHH volcano eruption. The HTHH submarine volcanic eruption also triggered an unusual tsunami, which can generate atmospheric gravity waves (Fig. 1014). We observed five strong group atmospheric waves associated with the HTHH volcano eruption from the ground-based airglow network observations.

The phase speed of the wave packet #1 is approximately ~~312-309~~ m/s, which is

observed almost simultaneously with the surface Lamb wave L0 mode. Wave packet #2, with average phase speed of ~~238–236~~ m/s, has been confirmed as Lamb wave L1 mode from theoretical prediction. Wave packet # 3 and wave packets #4-5 are generated by TIAPW and TITVE from backward ray tracing analysis. The horizontal phase speed distribution range of wave packets #3-5 is 200 m/s to 215 m/s, which is smaller than that of wave packets # 1-2. The horizontal phase speed of the wave packet #4-5 is less than that of the wave packet #1 and wave packet #2, which is approximately 207 m/s. For amplitude, the average amplitude of the lamb wave L1 mode (5.4%) is higher than that of the lamb wave L0 mode (3.2%), while wavepacket # 3, # 4, and # 5 have relatively small amplitudes, mainly distributed between 0.85% and 1.25%. The horizontal wavelengths of the atmospheric AGWs observed by the airglow network are very consistent with those of the tsunami near the coast. This is the first time that we observed the AGWs in the mesopause region triggered by the ~~tsunamis oceanic waves in the mesopause region~~ using optical detection equipment. It is also the first time to report atmospheric gravity waves excited by TIAPW.

~~The AGWs generated by TITVE propagate nearly 3000 km inland and almost covers the entire Chinese Mainland.~~ When the wave excited by TITVE propagate far away from the coast, the characteristics of AGWs are not consistent with the dispersion of free propagation AGWs. We find these wave packets are controlled by the duct, which can support the propagation of these GWs for thousands of kilometers after the tsunami were stopped at the coast. Therefore, ~~tsunamis ocean waves~~ can have a significant impact on the upper atmosphere over inland areas far from the ocean through AGWs.

508 The 2022 HTHH volcano eruption form a complex coupling relationship in the land-
509 ocean-atmosphere system (Fig. 14). Firstly, the heat released by the eruption has a direct
510 impact on the ocean, causing temperature changes in the surrounding waters. This can lead
511 to changes in the marine environment, affecting the behavior, distribution, and ecosystem
512 structure of organisms.

513 Meanwhile, volcanoes release gases such as carbon dioxide and sulfur dioxide.
514 Carbon dioxide is one of the greenhouse gases that can cause an increase in Earth's
515 temperature, leading to global warming. Sulfur dioxide can cause sulfuric acid mist in the
516 atmosphere, which affects the reflectivity and temperature of the atmosphere, and thus
517 affects the global climate.

518 Moreover, the 2022 HTHH volcano eruptions also trigger atmospheric waves and
519 tsunamis. The surface atmospheric pressure wave generated by the 2022 HTHH volcano
520 eruption can affect the upper atmosphere. The conventional tsunami triggered by the Tonga
521 volcano generated AGWs. The atmospheric pressure wave from the eruption generated a
522 fast tsunami never before observed by tsunami observation networks. When the tsunamis
523 reach the coast, their speeds decrease but their amplitudes increase, and the AGWs
524 generated by them will also affect the upper atmosphere. These AGWs play an important
525 coupling role between the ocean and the atmosphere by affecting the density and pressure
526 distribution of the atmosphere during propagation, leading to changes in the wind field and
527 affecting global atmospheric circulation. This study exhibits special dynamic coupling
528 process between air and sea via acoustic gravity waves (Fig. 14). This indirect impact on
529 the upper atmosphere provides a new perspective for us to study the coupling between the

ocean and the atmosphere and a key opportunity to improve the air-sea coupling model,
thereby enhancing our future ability to make tsunami warning forecasts.

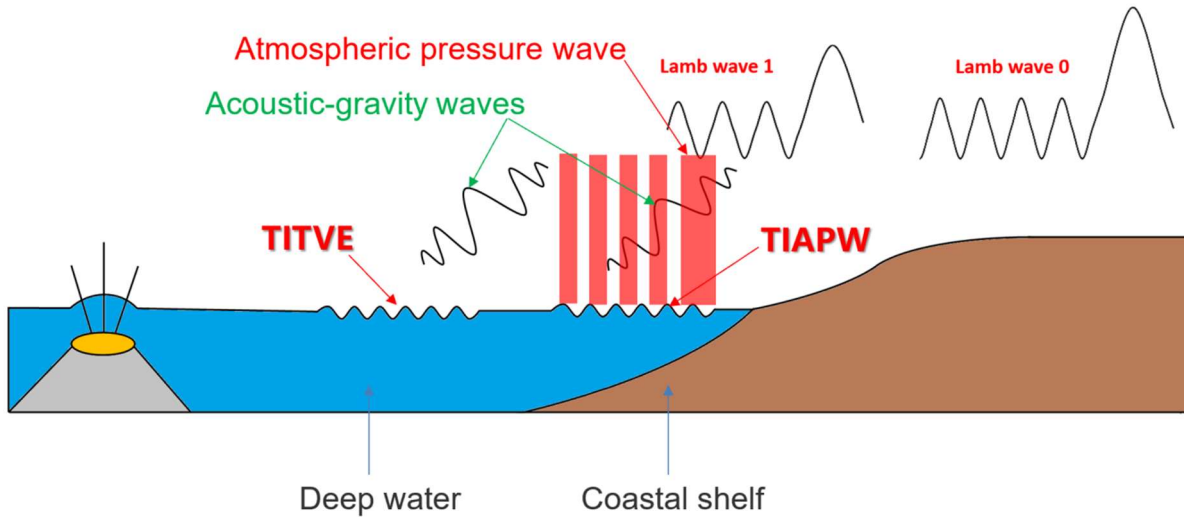


Figure 10-14 The Tonga volcano eruptions triggered two types of tsunamis, one type of tsunami is induced by the atmospheric pressure wave (TIAPW) and the other type tsunami is directly induced by the Tonga volcano eruption (TITVE). The acoustic gravity waves (AGWs) caused by tsunamis can propagate to the mesopause region.

Data availability

The ~~Multi-Double~~ Layer Airglow Network data is available at <https://data2.meridianproject.ac.cn/data> (MPDC, 2024). TIMED/SABER data is accessed from <http://saber.gats-inc.com/data.php> (last access: 10 January 2024). The ERA5 reanalysis data are able to be downloaded from the Copernicus Climate Change Service Climate Data Store through <https://www.ecmwf.int/en/forecasts/datasets/reanalysis-datasets/era5> (last access: 12 January 2024). Himawari-8 data are distributed by the Center for Environmental Remote Sensing (http://www.cr.chiba-u.jp/databases/GEO/H8_9/FD/index_en_V20190123.html) (last access: 20 January 2024).

Video supplements.

Multi-group of strong atmospheric waves observed over China associated with the 2022 Hunga Tonga–Hunga Ha’apai volcano eruptions (<https://doi.org/10.5446/66190> Li, 2024).
Animation series of OH airglow disturbances associated with the 2022 Hunga Tonga–Hunga Ha’apai volcano eruptions (https://doi.org/10.5446/s_1689 Li, 2024). A strong wave front observed by an OI 630 nm airglow imager over China associated with the 2022 Hunga Tonga–Hunga Ha’apai volcano eruptions (<https://doi.org/10.5446/66280> Li, 2024).

Author contributions

J.X and Q.L. conceived the idea of the manuscript. Q.L. carried out the data analysis, interpretation and manuscript preparation. A.R.G. developed and performed the numerical simulations. W.L and Y.Z compiled, processed and analysed satellite data. H.L.L., X.L and W.Y. contributed to the data interpretation and manuscript preparation. All authors discussed the results and commented on the manuscript.

Competing interests

The authors declare no competing interests.

Acknowledgements

This work was supported by the National Science Foundation of China (42374205, 41831073, and 41974179). The project is also supported by the Specialized Research Fund

for State Key Laboratories. We acknowledge the use of data from the Chinese Meridian Project.

References

Adam, D.: Tonga volcano eruption created puzzling ripples in Earth's atmosphere, *Nature*, 601, 497, <https://www.nature.com/articles/d41586-022-00127-1>, 2022.

Amores, A., Monserrat, S., Marcos, M., Argüeso, D., Villalonga, J., Jordà, G., and Gomis, D.: Numerical simulation of atmospheric Lamb waves generated by the 2022 Hunga-Tonga volcanic eruption, *Geophysical Research Letters*, 49, <https://doi.org/10.1029/2022GL098240>, 2022.

Astafyeva, E., Maletckii, B., Mikesell, T. D., Munaibari, E., Ravanelli, M., Coisson, P., et al. The 15 January 2022 Hunga Tonga eruption history as inferred from ionospheric observations, *Geophysical Research Letters*, 49, <https://doi.org/10.1029/2022GL098827>, 2022.

Azeem, I., Vadas, S. L., Crowley, G., and Makela, J. J.: Traveling ionospheric disturbances over the United States induced by gravity waves from the 2011Tohoku tsunami and comparison with gravity wave dissipative theory, *J. Geophys. Res. Space Physics*, 122, 3430–3447, <https://doi.org/10.1002/2016JA023659>, 2017.

Beer, T. *Atmospheric Waves*, 300 pp., John Wiley, New York, 1974.

Carvajal, M., Sepúlveda, I., Gubler, A., and Garreaud, R.: Worldwide signature of the 2022 Tonga volcanic tsunami, *Geophysical Research Letters*, 49(6), <https://doi.org/10.1029/2022GL098153>, 2022.

Donn, W. L., and Balachandran, N. K.: Mount St. Helens eruption of 18 May 1980: Air waves and explosive yield, *Science* 213, 539 – 541,

<https://doi.org/10.1126/science.213.4507.539>, 1981.

[Duncombe, J.: The surprising reach of Tonga's Giant atmospheric waves, Eos, 103, 2022.](#)

~~Drob, D. P., Emmert, J. T., Meriwether, J. W., Makela, J. J., Doornbos, E., Conde, M.,
Hernandez, G., Noto, J., Zawdie, K. A., McDonald, S. E., Huba, J. D., and Klenzing, J.
H.: An update to the Horizontal Wind Model (HWM): The quiet time thermosphere,
Earth and Space Science, 2, 301–319, 2015.~~

Duncombe, J.: The surprising reach of Tonga's Giant atmospheric waves, Eos, 103,
<https://doi.org/10.1029/2022EO220050>, 2022.

~~Fritts, D. C., and Alexander, M. J.: Gravity wave dynamics and effects in the middle
atmosphere, Rev. Geophys., 41, 1003, 2003.~~

Francis, S. H.: Acoustic-gravity modes and large-scale traveling ionospheric disturbances of
a realistic, dissipative atmosphere, J. Geophys. Res., 78 (13), 2278–2301,
<https://doi.org/10.1029/JA078i013p02278>, 1973.

[Garcia, F. J., Taylor, M. J., and Kelley, M. C.: Two-dimensional spectral analysis of
mesospheric airglow image data, Appl. Optics, 36 \(29\), 7374–7385,
<https://doi.org/10.1364/AO.36.007374>, 1997.](#)

Ghent, J. N., and Crowell, B. W.: Spectral characteristics of ionospheric disturbances over
the southwestern Pacific from the 15 January 2022 Tonga eruption and tsunami,
Geophysical Research Letters, 49, <https://doi.org/10.1029/2022GL100145>, 2022.

[Gossard, E. E., and Hooke, W. H.: Waves in the Atmosphere, Elsevier, Amsterdam, 1975,
456.](#)

[Grawe, M. A., and Makela, J. J.: The ionospheric responses to the 2011 Tohoku, 2012](#)

Haida Gwaii, and 2010 Chile tsunamis: Effects of tsunami orientation and observation geometry, Earth and Space Science, 2, 472–483, <https://doi.org/10.1002/2015EA000132>, 2015.

Grawe, M. A., and Makela, J. J.: Observation of tsunami-generated ionospheric signatures over Hawaii caused by the 16 September 2015 Illapel earthquake, J. Geophys. Res. Space Physics, 122, 1128–1136, <https://doi.org/10.1002/2016JA023228>, 2017.

Gusman, A.R., Roger, J., Noble, C. et al. The 2022 Hunga Tonga-Hunga Ha’apai Volcano Air-Wave Generated Tsunami, Pure and Applied Geophysics, 179, 3511–3525, <https://doi.org/10.1007/s00024-022-03154-1>, 2022.

Harkrider, D., and Press, F.: The Krakatoa air-sea waves: An example of pulse propagation in coupled systems, Geophys. J. R. Astron. Soc. 13, 149 – 159, <https://doi.org/10.1111/j.1365-246X.1967.tb02150.x>, 1967.

Hersbach, H., Bell, B., Berrisford, P., Hirahara, S., Horányi, A., Muñoz-Sabater, J., Nicolas, J., Peubey, C., Radu, R., Schepers, D., Simmons, A., Soci, C., Abdalla, S., Abellan, X., Balsamo, G., Bechtold, P., Biavati, G., Bidlot, J., Bonavita, M., De Chiara, G., Dahlgren, P., Dee, D., Diamantakis, M., Dragani, R., Flemming, J., Forbes, R., Fuentes, M., Geer, A., Haimberger, L., Healy, S., Hogan, R. J., Hólm, E., Janisková, M., Keeley, S., Laloyaux, P., Lopez, P., Lupu, C., Radnoti, G., deRosnay, P., Rozum, I., Vamborg, F., Villaume, S., and Thépaut, J. N. The ERA5 global reanalysis, Q. J. R. Meteorol. Soc., 146, 1999–2049, <https://doi.org/10.1002/qj.3803>, 2020 (data available at: <https://www.ecmwf.int/en/forecasts/datasets/reanalysis-datasets/era5> last access: 12 January 2024).

637 Hickey, M. P., Schubert, G., and Walterscheid, R. L.: Propagation of tsunami-driven
638 gravity waves into the thermosphere and ionosphere, *J. Geophys. Res.*, 114,
639 <https://doi.org/10.1029/2009JA014105>, 2009.

640 Hickey, M. P., Schubert, G., and Walterscheid, R. L.: Atmospheric airglow fluctuations due
641 to a tsunami-driven gravity wave disturbance, *Journal of Geophysical Research*,
642 115(A6), A06308, <https://doi.org/10.1029/2009JA014977>, 2010.

643 Hines, C.: Gravity waves in the atmosphere, *Nature*, 239 (5367), 73–78,
644 <https://doi.org/10.1038/239073A0>, 1972.

645 Inchin, P. A., Heale, C. J., Snively, J. B., and Zettergren, M. D.: The dynamics of nonlinear
646 atmospheric acoustic-gravity waves generated by tsunamis over realistic bathymetry,
647 *Journal of Geophysical Research: Space Physics*, 125,
648 <https://doi.org/10.1029/2020JA028309>, 2020.

649 Inchin, P. A., Heale, C. J., Snively, J. B., and Zettergren, M.D.: Numerical modeling of
650 tsunami-generated acoustic-gravity waves in mesopause airglow, *Journal of*
651 *Geophysical Research: Space Physics*, 127, <https://doi.org/10.1029/2022JA030301>,
652 2022.

653 ~~Kanamori, H., and Given, J. W.: Lamb pulse observed in nature, *Geophys. Res. Lett*, 10,~~
654 ~~373–376, 1983.~~

655 Koketsu K. and Higashi S.: Three-dimensional topography of the sediment/basement
656 interface in the Tokyo Metropolitan area, Central Japan, *Bull. seism. Soc. Am.*, 82,
657 2328–2349, <https://doi.org/10.1785/BSSA0820062328>, 1992.

658 Kubota, T., Saito, T., & Nishida, K.: Global fast-traveling tsunamis driven by atmospheric

- Lamb waves on the 2022 Tonga eruption, *Science*, 377, 91-94,
<https://doi.org/10.1126/science.abo4364>, 2022.
- Laughman, B., Fritts, D. C., and Lund, T. S.: Tsunami-driven gravity waves in the presence
of vertically varying background and tidal wind structures, *J. Geophys. Res. Atmos.*,
122, 5076-5096, <https://doi.org/10.1002/2016JD025673>, 2017.
- Li, X., Ding, F., Yue, X., Mao, T., Xiong, B., and Song, Q.: Multiwave structure of
traveling ionospheric disturbances excited by the Tonga volcanic eruptions observed
by a dense GNSS network in China, *Space Weather*, 21,
<https://doi.org/10.1029/2022SW003210>, 2023.
- Lighthill, M. J.: *Waves in Fluids*, Cambridge University Press, Cambridge, UK, New York,
504 pp., ISBN: 0-521-01045-4, 1978.
- Lin, J.-T., Rajesh, P. K., Lin, C. C. H., Chou, M.-Y., Liu, J.-Y., Yue, J., et al. Rapid
conjugate appearance of the giant ionospheric Lamb wave signatures in the northern
hemisphere after Hunga-Tonga volcano eruptions, *Geophysical Research Letters*, 49,
<https://doi.org/10.1029/2022GL098222>, 2022.
- Lindzen, R. S., and Blake, D.: Lamb waves in the presence of realistic distributions of
temperature and dissipation, *Journal of Geophysical Research*, 77(12), 2166 – 2176,
<https://doi.org/10.1029/JC077i012p02166>, 1972.
- Li, Q., Xu, J., Liu, H., Liu, X., and Yuan, W.: How do gravity waves triggered by a typhoon
propagate from the troposphere to the upper atmosphere?. *Atmos. Chem. Phys.*, 22,
12077–12091, <https://doi.org/10.5194/acp-22-12077-2022>, 2022.
- Li, Q.: Multi-group of strong atmospheric waves observed over China associated with the

2022 Hunga Tonga–Hunga Ha’apai volcano eruptions, TIB AV-Portal [video],
<https://doi.org/10.5446/66190>, 2024.

Li, Q.: Animation series of OH airglow disturbances associated with the 2022 Hunga
Tonga–Hunga Ha’apai volcano eruptions, TIB AV-Portal [video],
https://doi.org/10.5446/s_1689, 2024.

Li, Q.: A strong wave front observed by an OI 630 nm airglow imager over China
associated with the 2022 Hunga Tonga–Hunga Ha’apai volcano eruptions, TIB
AV-Portal [video], <https://doi.org/10.5446/66280>, 2024.

Liu, H.-L., Wang, W., Huba, J.D., Lauritzen, P. H., and Vitt, F. Atmospheric and
Ionospheric Responses to Hunga-Tonga Volcano Eruption Simulated by WACCM-X,
Geophysical Research Letters, 50, <https://doi.org/10.1029/2023GL103682>, 2023.

Liu, X., Xu, J., Yue, J., and Kogure, M.: Strong gravity waves associated with Tonga
volcano eruption revealed by SABER observations, Geophysical Research Letters, 49,
<https://doi.org/10.1029/2022GL098339>, 2022.

Makela, J. J., Lognonné, P., Hébert, H., Gehrels, T., Rolland, L., Allgeyer, S., et al. Imaging
and modeling the ionospheric airglow response over Hawaii to the tsunami generated by
the Tohoku earthquake of 11 March 2011, Geophysical Research Letters, 38 (24),
<https://doi.org/10.1029/2011GL047860>, 2011.

MPDC: Airglow data [data set], <https://data2.meridianproject.ac.cn/data>, last access: 15
January 2024.

Nishikawa, Y., Yamamoto, My., Nakajima, K. et al. Observation and simulation of
atmospheric gravity waves exciting subsequent tsunami along the coastline of Japan

after Tonga explosion event, *Sci Rep* 12, 22354, <https://doi.org/10.1038/s41598-022-25854-3>, 2022.

Occhipinti, G., Rolland, L., Lognonné, P., and Watada, S.: From Sumatra 2004 to Tohoku-Oki 2011: The systematic GPS detection of the ionospheric signature induced by tsunamigenic earthquakes, *Journal of Geophysical Research: Space Physics*, 118, 3626–3636, <https://doi.org/10.1002/jgra.50322>, 2013.

Omira, R., Ramalho, R.S., Kim, J. et al. Global Tonga tsunami explained by a fast-moving atmospheric source, *Nature* 609, 734–740, <https://doi.org/10.1038/s41586-022-04926-4>, 2022.

Otsuka, S.: Visualizing Lamb waves from a volcanic eruption using meteorological satellite Himawari-8. *Geophysical Research Letters*, 49, <https://doi.org/10.1029/2022GL098324>, 2022 (data available at: http://www.cr.chiba-u.jp/databases/GEO/H8_9/FD/index_en_V20190123.html last access: 20 January 2024).

Peltier, W., and Hines, C.: On the possible detection of tsunamis by a monitoring of the ionosphere, *Journal of Geophysical Research*, 81(12), 1995–2000, <https://doi.org/10.1029/JC081i012p01995>, 1976.

Poblet, F. L., Chau, J. L., Conte, J. F., Vierinen, J., Suclupe, J., Liu, A., and Rodriguez, R. R.: Extreme horizontal wind perturbations in the mesosphere and lower thermosphere over South America associated with the 2022 Hunga eruption, *Geophysical Research Letters*, 50, <https://doi.org/10.1029/2023GL103809>, 2023.

Pradipta, R., Carter, B. A., Currie, J. L., Choy, S., Wilkinson, P., Maher, P., and Marshall, R.: On the propagation of traveling ionospheric disturbances from the Hunga Tonga-Hunga

Ha'apai volcano eruption and their possible connection with tsunami waves,
 Geophysical Research Letters, 50, <https://doi.org/10.1029/2022GL101925>, 2023.

[Press, F., and Harkrider, D. G.: “Propagation of acoustic-gravity waves in the atmosphere,” J. Geophys. Res. 67, 3889–3908, 1962.doi:10.1029/JZ067i010p03889.](#)

Salmon, R.: Introduction to ocean waves, Scripps Inst. of Oceanogr., Univ. of Calif., San Diego., 2014.

[Sepúlveda, I., Carvajal, M., and Agnew, D. C.: Global winds shape planetary-scale Lamb waves. Geophysical Research Letters, 50, <https://doi.org/10.1029/2023GL106097>, 2023](#)

Smith, S.M., Martinis, C. R., Baumgardner, J., and Mendillo, M.: All-sky imaging of transglobal thermospheric gravity waves generated by the March 2011 Tohoku Earthquake, J. Geophys. Res. Space Physics, 120, 10,992–10,999, <https://doi.org/10.1002/2015JA021638>, 2015.

[Swenson, G. R. and Mende, S. B.: OH emission and gravity waves \(including a breaking wave\) in all-sky imagery from Bear Lake, UT, Geophys. Res. Lett., 21, 2239–2242, <https://doi.org/10.1029/94GL02112>, 1994.](#)

Symons, G. J.: The Eruption of Krakatoa, and Subsequent Phenomena: Report of the Krakatoa Committee of the Royal Society (Wiley Online Library), 1888.

[Takahashi, H., Figueiredo, C.A.O.B., Barros, D. et al. Ionospheric disturbances over South America related to Tonga volcanic eruption, Earth Planets Space 75, 92, <https://doi.org/10.1186/s40623-023-01844-1>, 2023.](#)

[Tang, J., Kamalabadi, F., Franke, S. J., Liu, A. Z., and Swenson, G. R.: Estimation of gravity wave momentum flux with spectroscopic imaging, IEEE T. Geosci. Remote, 43,](#)

103–109, <https://doi.org/10.1109/TGRS.2004.836268>, 2005.

Themens, D. R., Watson, C., Zagar, N., Vasylykevych, S., Elvidge, S., McCaffrey, A., et al.
Global propagation of ionospheric disturbances associated with the 2022 Tonga
volcanic eruption, *Geophysical Research Letters*, 49(7),
<https://doi.org/10.1029/2022GL098158>, 2022.

Vadas, S. L., Makela, J. J., Nicolls, M. J., and Milliff, R. F.: Excitation of gravity waves by
ocean surface wave packets: Upward propagation and reconstruction of the
thermospheric gravity wave field, *J. Geophys. Res. Space Physics*, 120, 9748–9780,
<https://doi.org/10.1002/2015JA021430>, 2015.

~~Wright, C.J., et al. Surface to space atmospheric waves from Hunga Tonga Hunga Ha'apai
eruption, *Nature*, 609 (7928), 741–746, 2022.~~

Xu, J., Li, Q., Sun, L., Liu, X., Yuan, W., Wang, W., Yue, J., Zhang, S., Liu, W., Jiang, G.,
Wu, K., Gao, H., and Lai, C.: The Ground - Based Airglow Imager Network in China:
Recent Observational Results, *Geophysical Monograph Series*, 261, 365-394,
<https://doi.org/10.1002/9781119815631.ch19>, 2021.

Xu, J., et al. Concentric gravity waves over northern China observed by an airglow imager
network and satellites, *J. Geophys. Res. Atmos.*, 120, 11,058–11,078,
<https://doi.org/10.1002/2015JD023786>, 2015.

Yamada, M., Ho, T.-C., Mori, J., Nishikawa, Y., and Yamamoto, M.-Y.: Tsunami triggered
by the Lamb wave from the 2022 Tonga volcanic eruption and transition in the
offshore Japan region, *Geophysical Research Letters*, 49,
<https://doi.org/10.1029/2022GL098752>, 2022.

Yeh, K. C., and Liu, C. H.: Acoustic-Gravity Waves in the Upper Atmosphere, Reviews of
Geophysics and Space Physics, 12 (2), 193, <https://doi.org/10.1029/RG012i002p00193>,
1974.

Wrasse, C. M., Nakamura, T., Tsuda, T., Takahashi, H., Medeiros, A. F., Taylor, M.
J., Gobbi, D., Salatun, A., Suratno, E. A., and Admiranto, A. G.: Reverse ray tracing of
the mesospheric gravity waves observed at 23°S (Brazil) and 7°S (Indonesia) in airglow
imagers, J. Atmos. Sol. Terr. Phys., 68, 163–181,
<https://doi.org/10.1016/j.jastp.2005.10.012>, 2006.

[Wright, C.J., et al. Surface-to-space atmospheric waves from Hunga Tonga-Hunga Ha’apai
eruption, Nature, 609 \(7928\), 741–746, https://doi.org/10.1038/s41586-022-05012-5,
2022.](https://doi.org/10.1038/s41586-022-05012-5)

Zhang, S., Vierinen, J., Aa, E., Goncharenko, L. P., Erickson, P., Rideout, W., et al. 2022
Tonga volcanic eruption induced global propagation of ionospheric disturbances via
Lamb waves, Frontiers in Astronomy and Space Sciences, 9, 1–10,
<https://doi.org/10.3389/fspas.2022.871275>, 2022.